Spin-singlet formation in the spin-tetramer layered organic-inorganic hybrid $CH_3NH_3Cu_2Cl_5$

Machteld E. Kamminga,[1,*] Maria Azhar,[1] Julian Zeisner,[2,3] Anna M. C. Maan,[1] Bernd Büchner,[2,3] Vladislav Kataev,[2] Jacob Baas,[1] Graeme R. Blake,[1] Maxim Mostovoy,[1] and Thomas T. M. Palstra[1]

[1]*Zernike Institute for Advanced Materials, University of Groningen, Nijenborgh 4, 9747 AG Groningen, The Netherlands*

[2]*Leibniz Institute for Solid State and Materials Research, IFW Dresden, 01069 Dresden, Germany*

[3]*Institut für Festkörper- und Materialphysik, Technische Universität Dresden, 01062 Dresden, Germany*

(Received 24 April 2018; published 18 June 2018)

We report spin-singlet formation in an organic-inorganic hybrid identified as $CH_3NH_3Cu_2Cl_5$. The hybrid adopts a layered structure in which $Cu_2Cl_5^-$ layers are separated by $CH_3NH_3^+$ layers. The inorganic layers consist of corner- and edge-sharing $CuCl_6$ octahedra, forming edge-sharing tetramers. Magnetic susceptibility measurements indicate strong antiferromagnetic interactions within the tetramers, whereas the coupling between the tetramers is weak. Low-temperature magnetic susceptibility data as well as electron spin resonance measurements suggest a nonmagnetic ground state with a large spin gap of ∼130 K, in apparent contradiction with ferromagnetic interactions between nearest-neighbor spins. We discuss a spin-tetramer model in which antiferromagnetic next-nearest-neighbor interactions lead to a spin-singlet state.

DOI: 10.1103/PhysRevMaterials.2.064405

I. INTRODUCTION

Organic-inorganic hybrid perovskites, with structural formula ABX_3, are of much interest for a broad range of applications because of interesting magnetic [1–8], ferroelectric [9,10], conducting [11–15], optical [16,17], and optoelectronic [18–24] properties of these materials. Hybrid perovskite structures generally consist of organic cations A that occupy the 12-fold coordinated sites, coordinated by metal halide BX_6 octahedra. In addition to the three-dimensional (3D) perovskites, layered perovskite structures with structural formula A_2BX_4 can be obtained. These layered hybrids consist of single ⟨100⟩-terminated perovskite sheets separated by bilayers of the organic cations and are held together by the van der Waals interactions between the organic groups [13].

From the early 1970s, long-range magnetic order has been studied in layered hybrid perovskites incorporating Fe^{2+}, Mn^{2+}, Cu^{2+}, and Cr^{2+} as the metal cation, B [3–7]. The magnetic properties are determined by the magnetic superexchange interactions through the B-X-B bonds (where X is the halogen). Furthermore, incorporation of Jahn-Teller (JT) active metal cations has a major influence on the perovskite structure and therefore on the magnetic properties. Layered hybrid perovskites based on Mn^{2+} and Fe^{2+} cations do not exhibit JT distortions and have B-X-B angles of ∼ 180°. Following the Goodenough-Kanamori rules [25,26], these hybrids exhibit antiferromagnetic (AFM) interactions [3–5]. Cu^{2+} and Cr^{2+}, on the other hand, are JT active. These distortions result in orthogonal electronic orbitals of adjacent metal ions, giving rise to ferromagnetic (FM) superexchange via a 180° pathway [6,7,27]. A textbook example is methylammonium copper chloride, $(CH_3NH_3)_2CuCl_4$, which exhibits FM order below $T_c = 8.9$ K [3,28].

In this work, we investigate the synthesis and magnetic properties of a new methylammonium copper chloride compound: $CH_3NH_3Cu_2Cl_5$ (hereafter **1**). Similar to $(CH_3NH_3)_2CuCl_4$ (hereafter **2**), **1** is a layered structure in which inorganic sheets are separated by organic cations. However, the inorganic $Cu_2Cl_5^-$ layers consist of a unique pattern of corner- and edge-sharing $CuCl_6$ octahedra. Our static magnetic susceptibility measurements as well as electron spin resonance (ESR) data reveal that this connectivity of JT-distorted octahedra results in a broad maximum in the temperature dependence of the magnetic susceptibility, $\chi(T)$, at around 82 K and a spin-singlet state with a spin gap of ∼130 K. These results are very surprising, as the crystal structure analysis indicates that the nearest-neighbor exchange interactions are ferromagnetic and weak. From the fit of $\chi(T)$ with a model of isolated tetramers of edge-sharing $CuCl_6$ octahedra, we obtain an estimate for the spin gap and the strongest antiferromagnetic exchange interactions. In contrast to other materials with four-spin building blocks, such as $Cu_2Fe_2Ge_4O_{13}$ [29] and $Cu_2CdB_2O_6$[30], spins in the title compound do not show any sign of long-range order. The unique feature of this material is the microscopic mechanism for the spin-singlet ground state, which originates from strong next-nearest-neighbor exchange interactions between Cu spins in the tetramers. The crystal chemistry of layered methylammonium copper chlorides thus allows for a design beyond corner sharing involving edge-sharing units, resulting in a two-dimensional (2D) crystal structure with a singlet magnetic ground state.

II. EXPERIMENT

Single crystals of **1** were grown from slow evaporation of an equimolar mixture of CH_3NH_2, HCl, and $CuCl_2 \cdot 2H_2O$, dissolved in EtOH. Besides the compound of interest, yellow sheets of the prototypical layered hybrid phase, **2**, were obtained as well. 1.70 g (10 mmol) of $CuCl_2 \cdot 2H_2O$ (Alfa Aesar;

*Corresponding author: m.e.kamminga@rug.nl

99%) was placed in an Erlenmeyer flask upon addition of 30 ml of EtOH (J.T. Baker) and swirled until fully dissolved and a dark-green clear solution was obtained. 0.82 ml (10 mmol) of HCl (37 wt% in H_2O; Boom) was added without color change. Upon adding 1.35 ml (10 mmol) of CH_3NH_2 solution (33 wt% in EtOH; Sigma Aldrich), immediate crystallization of yellow crystals took place. A small amount of the crystals were extracted and identified as the **2** phase [31,32], using x-ray diffraction. The flask was covered in Parafilm, to prevent evaporation, and placed in the oven at 50 °C overnight to increase the solubility. The next day, 20 ml of clear solution was separated from the crystals in the Erlenmeyer flask (flask A) and placed in a new flask (flask B). Both flasks were covered with Parafilm, containing four small holes for slow evaporation, and placed back in the oven at 50 °C. All products were obtained after 1 week, when all remaining liquid had evaporated. Flask A contained brown **1** crystals and the previously formed yellow **2** crystals. Flask B contained the brown **1** crystals and turquoise needles, which we identified as a recrystallization of the starting compound $CuCl_2 \cdot 2H_2O$, using x-ray diffraction. Supplemental Material Fig. S1 shows a photograph of the products of flask A and flask B [33]. The brown crystals are bar shaped and small, with the majority having dimensions less than 1 mm. The crystals were stored under low-humidity conditions in a dry box. Figure S2 shows an optical microscope image of as-grown crystals [33].

Single-crystal x-ray diffraction (XRD) measurements were performed using a Bruker D8 Venture diffractometer equipped with a Triumph monochromator and a Photon100 area detector, operating with Mo $K\alpha$ radiation. The crystals were mounted on a 0.3-mm nylon loop, using cryo-oil. A nitrogen flow from an Oxford Cryosystems Cryostream Plus was used to cool the crystals. Data processing was done using the Bruker APEX III software. The SHELX97 software [34] was used for structure solution and refinement.

A Quantum Design XL MPMS SQUID magnetometer was used to carry out magnetic measurements. Polycrystalline samples of **1** (6.4 mg) and **2** (3.7 mg) were investigated. The measurements of the magnetization versus applied magnetic field were performed at 5 K. The measurements of the magnetization versus temperature were performed under an applied magnetic field of 0.1, 0.5, and 1 T (zero-field cooled).

Electron spin resonance (ESR) measurements were conducted using a Bruker EMX X-band spectrometer, which operates at a microwave frequency of 9.6 GHz and is equipped with an ESR900 gas flow cryostat (Oxford Instruments). ESR experiments were performed on a small crystal as well as on a powder sample of **1**, yielding similar results for both samples. In addition, a small crystal of **2** was measured as reference to identify the lines caused by the FM contamination of **1**.

III. RESULTS AND DISCUSSION

We have synthesized high-quality single crystals of **1**, and studied its crystal structure and magnetic properties. **1** is an organic-inorganic hybrid, in which the organic and inorganic constituents are present in a 1:2 ratio. This is not the most common stoichiometry found in hybrid perovskites. Most known layered perovskites yield the general formula A_2BX_4, where A is a protonated primary amine, B a divalent metal, and X a halide [35]. These structures consist of single ⟨100⟩-terminated $CuCl_4^{2-}$ sheets separated by bilayers of $CH_3NH_3^+$ and held together through van der Waals interactions [13]. In the case of the methylammonium copper chloride hybrids, this would mean $(CH_3NH_3)_2CuCl_4$ (**2**). **2** is an existing form that grows as yellow sheetlike crystals. This compound has already been studied decades ago as a textbook 2D magnet [3,28,31,32]. Therefore, we focus here on compound **1**, and its properties. This AB_2X_5 stoichiometry has been observed in another copper chloride hybrid as well [36]. However, the $[(CH_3)_4P]Cu_2Cl_5$ compound yields a different structure than our compound of interest. **1** exhibits structural features that we have not encountered in literature, and we will discuss its structure in more detail below. Notably, during synthesis of **1**, we found that the yellow **2** phase always forms as well. The synthesis procedure is explained in more detail in the Supplemental Material [33].

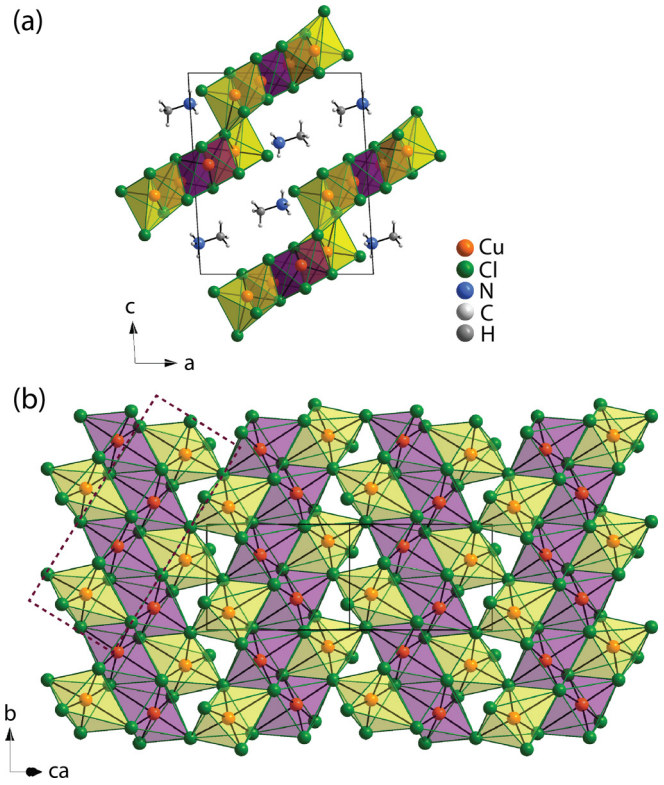

FIG. 1. Polyhedral model of **1**, projected along the [010] direction (a), and a single inorganic sheet projected along the $[\bar{1}01]$ direction, to provide a top view of a single sheet (b). The yellow and purple shadings represent octahedra around the two crystallographically distinct copper ions, Cu1 and Cu2, respectively. The dashed box indicates a tetramer of edge-sharing $CuCl_6$ octahedra. Due to JT distortion, all $CuCl_6$ octahedra are elongated in the direction perpendicular to the tetramer chain formation.

Figure 1 shows the crystal structure of **1**. As stated above, the crystals grow bar shaped. Our analysis revealed that the longest axis is the b axis. This is the most favorable growth direction. The refinement was done in the monoclinic space group $P2_1/n$, without any twinning present. The crystallographic and refinement parameters are given in Table I. Our single-crystal XRD measurements show that the crystals have the same structural phase at room temperature as at 100 K. The

TABLE I. Crystallographic and refinement parameters of $CH_3NH_3Cu_2Cl_5$. The measurements are performed using Mo $K\alpha$ radiation (0.710 73 Å). Full-matrix least-squares refinement against F^2 was carried out using anisotropic displacement parameters. A multiscan absorption correction was performed. Hydrogen atoms were added by assuming a regular tetrahedral coordination to carbon and nitrogen, with equal bond angles and fixed distances.

	$CH_3NH_3Cu_2Cl_5$
Temperature (K)	100(2)
Formula	$CH_6NCu_2Cl_5$
Formula weight (g/mol)	336.40
Crystal size (mm^3)	0.08×0.04×0.02
Crystal color	Brown
Crystal system	Monoclinic
Space group	$P2_1/n$ (No. 14)
Symmetry	Centrosymmetric
Z	4
D (calculated) (g/cm^3)	2.506
$F(000)$	648
a (Å)	11.2080(11)
b (Å)	6.0995(6)
c (Å)	13.0688(12)
α (°)	90.0
β (°)	93.526(4)
γ (°)	90.0
Volume ($Å^3$)	891.73(15)
μ (mm^{-1})	6.183
min/max transmission	0.0775/0.1254
θ range (°)	3.12–26.43
Index ranges	$-14 < h < 14$
	$-7 < k < 7$
	$-16 < l < 16$
Data/restraints/parameters	1830/0/84
GooF of F^2	1.078
No. total reflections	31 099
No. unique reflections	1830
No. obs Fo > 4σ(Fo)	1643
R1 [Fo > 4σ(Fo)]	0.0135
R1 (all data)]	0.0185
wR2 [Fo > 4σ(Fo)]	0.0293
wR2 (all data)	0.0306
Largest peak and hole ($e/Å^3$)	0.28 and −0.32

asymmetric unit of **1** is shown in Fig. S3 [33]. **1** has a 2D structure in which $Cu_2Cl_5^-$layers are separated by $CH_3NH_3^+$. Notably, the inorganic layers consist of both corner- and edge-sharing $CuCl_6$ octahedra [see Fig. 1(b)]. In fact, the structure consists of tetramers of edge-sharing $CuCl_6$ octahedra containing two crystallographically inequivalent Cu^{2+} ions. Three octahedra of each tetramer share edges with the octahedra of a neighboring tetramer, thus forming ribbons. These ribbons are connected to each other by corner sharing, to build a "staircase" 2D sheet, as shown in Fig. 1(a). The JT instability of Cu^{2+} ions with nine d electrons gives rise to an elongation of $CuCl_6$ octahedra as shown Fig. 1(b). The physical consequence of this distortion will be discussed in more detail below.

As stated in the Supplemental Material [33], it was impossible to grow **1** without growing **2** as well. For single-crystal XRD measurements, it is possible to select single crystals of **1** from the mixture. However, due to the small size of the crystals, we used an aggregate of many small crystals for the magnetic measurements. While we made a great effort to separate the two phases, we found it impossible to obtain a large enough polycrystalline sample of **1** without a small contamination by **2**. Given the weight of both samples and their magnetic response (see Figs. S4 and S5 [33]), we calculated that the **1** sample has a small **2** contamination of 1.49 wt%. As **2** has one Cu^{2+} per formula unit and 1 has two, a simple calculation shows that in the contaminated **1** sample, 1% of all Cu^{2+} are in the FM **2** phase.

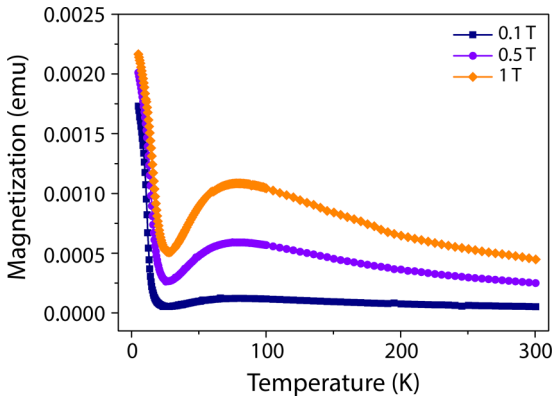

FIG. 2. Magnetization as a function of temperature measured in various applied magnetic fields (zero-field cooled) of a polycrystalline sample of **1** with a small contamination of **2**.

Figure 2 shows the magnetization of the **1** sample as a function of temperature in various applied magnetic fields. Two types of behavior are apparent from this graph: a FM contribution at low temperatures (see Fig. S4 [33]) and a broad maximum at around 82 K. We ascribe the low-temperature feature to the contaminant **2**. The amplitude of the contribution shows a broad maximum that scales with applied magnetic field, whereas the FM contribution reaches saturation above 0.1 T. Therefore, we attribute this "bump" to the **1** phase. This conclusion is consistent with the assumption that the FM contribution originates from the 1.49 wt% contamination of **2**, as discussed in the Supplemental Material [33]. Furthermore, the appearance of this broad maximum at around 82 K indicates strong antiferromagnetic exchange interactions in **1**. The proposed model for the magnetic interactions is discussed below.

In Fig. 3, we obtained the magnetic susceptibility of the **1** sample by subtracting the magnetic susceptibility of **2** (1.49 wt%), measured in the same applied field, from Fig. 2. Therefore, the corrected curve shows the magnetic response of the **1** phase. The broad maximum near 82 K is very pronounced. Notably, the susceptibility tends to zero as temperature decreases to 0 K, indicating a nonmagnetic ground state.

To support the validity of our approach (correction of the magnetic susceptibility of **1** for a small contamination of **2**), we performed ESR measurements on **1** (see Fig. 4) and **2** (see Fig. S6 [33]). ESR is advantageous in that it can spectroscopically resolve different contributions to the average static magnetic response. The intensities of the individual lines in the ESR spectrum are proportional to the static susceptibility

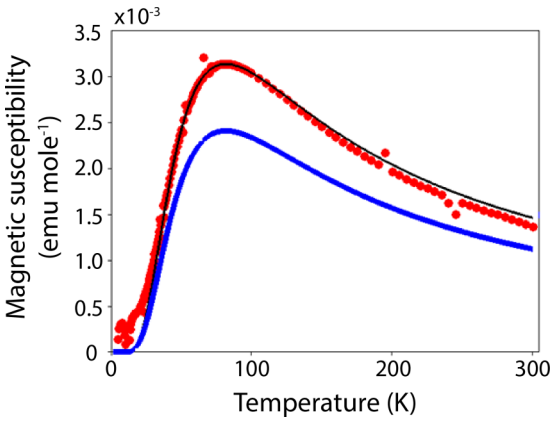

FIG. 3. Magnetic susceptibility as a function of temperature measured in 0.1 T (zero-field cooled) of a polycrystalline sample of **1** after subtracting a 1.49 wt% contamination of **2** (red circles). The black and blue lines correspond to the theoretical susceptibility based on the tetramer model, with and without normalization factor, respectively (see text).

of the resonating spin species. Indeed, as shown in Fig. 4, ESR resolves the spin states of **1** and contaminant **2**. At high temperatures, the spectrum consists of a single broad line. Upon lowering temperature, the intensity of the broad line increases and two further lines appear, which are narrower as compared to the main line. As shown in Fig. S6 [33], the broad line is absent in the ESR spectrum of **2**, proving that the signal corresponds to **1**, while the narrow lines are associated with **2**. Further evidence for the different origins of the broad and narrow lines was obtained from angular dependent measurements performed at 50 K (see Fig. S7 [33]).

At around 80 K the intensity of the broad line reaches a maximum, in agreement with the maximum of the static susceptibility in Fig. 3. Figure 5 shows that both experimental methods (magnetic measurements and ESR) yield the same temperature dependence of the susceptibility. Figure S8 shows a more elaborate comparison of the two techniques [33].

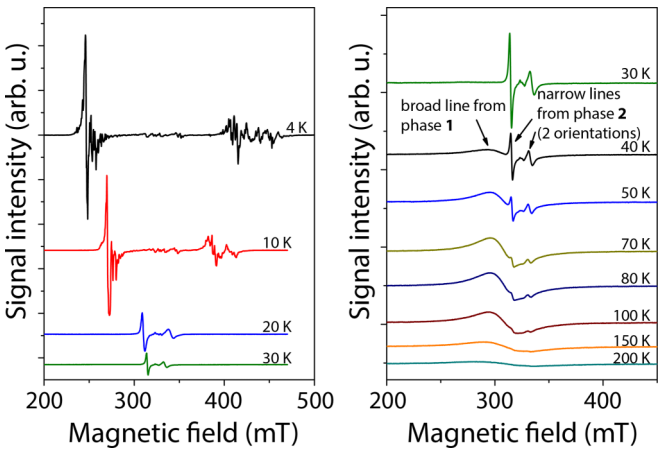

FIG. 4. ESR spectrum (magnetic field derivative of the absorption signal) at different temperatures, measured on a **1** crystal (contaminated with **2**) with magnetic field applied in plane with respect to the inorganic sheets. Spectra are shifted vertically for comparison.

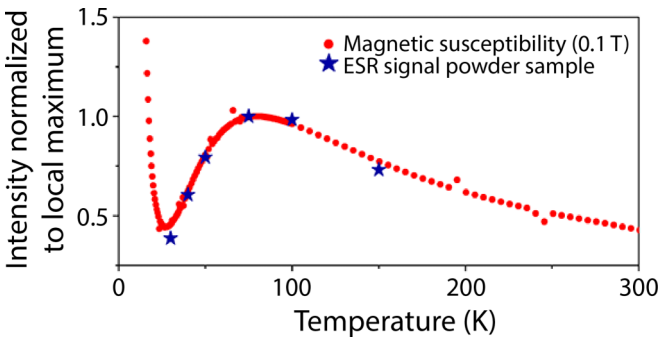

FIG. 5. Comparison of the magnetic susceptibility, measured at a field of 0.1 T, with the intensity obtained from ESR measurements in **1**. Intensities are obtained from double integration of the ESR spectra as a function of temperature. Data are normalized to the (local) maximum around 82 K. Notably, both experimental methods (magnetic measurements and ESR) yield the same temperature dependence of the susceptibility. Figure S8 shows a more elaborate comparison of the two techniques [33].

Further lowering the temperature yields a gradual decrease in intensity of the broad line. Finally this signal disappears below 30 K, whereas the intensities of the narrow lines continue to increase with decreasing temperature. The vanishing of the broad line at low temperatures gives further evidence for the nonmagnetic ground state of **1**. In the low-temperature region the spectrum comprises only the narrow lines which are shifted considerably from their position at higher temperatures and split into many lines. The splitting might be caused by small cracks in the crystal or small crystallites which are slightly misaligned, thereby leading to different resonance fields.

In order to understand the magnetic interactions, we propose a model based on the crystal structure. The Cu^{2+} ions in elongated $CuCl_6$ octahedra have one hole with spin 1/2 in the $d_{x^2-y^2}$ orbital, which lies in the xy plane perpendicular to the elongation axis. There are three types of superexchange interactions between neighboring $CuCl_6$ octahedra: between edge-sharing octahedra within a tetramer, between edge-sharing octahedra of neighboring tetramers forming ribbons, and between corner-sharing octahedra of neighboring ribbons. The orbital overlap in all three scenarios is illustrated in Fig. 6. The strongest interactions are within the tetramers owing to the large overlap of the $2p$ orbitals of Cl ions with the $d_{x^2-y^2}$ orbitals of two neighboring Cu ions. In contrast, the $d_{x^2-y^2}$ orbitals of Cu ions from different tetramers are hybridized with the p orbitals of different Cl ions, which makes the exchange interactions between tetramers very weak. Therefore, in our model tetramers are assumed to be magnetically decoupled.

In this respect, compound **1** is different from the well-studied spin-singlet material $SrCu_2(BO_3)_2$ [37–39]. The latter compound is described by a 2D orthogonal dimer Heisenberg model, which is topologically equivalent to the 2D Shastry-Sutherland model [40], which remains in the spin-singlet state even for relatively strong interactions between the dimers. The interdimer interactions result in strong reduction of the spin gap in $SrCu_2(BO_3)_2$, whereas in **1** the spin gap is of the order of the strongest antiferromagnetic exchange interaction, as shown below. The key issue is the difference between the dimensonalities of the crystal and magnetic structure in

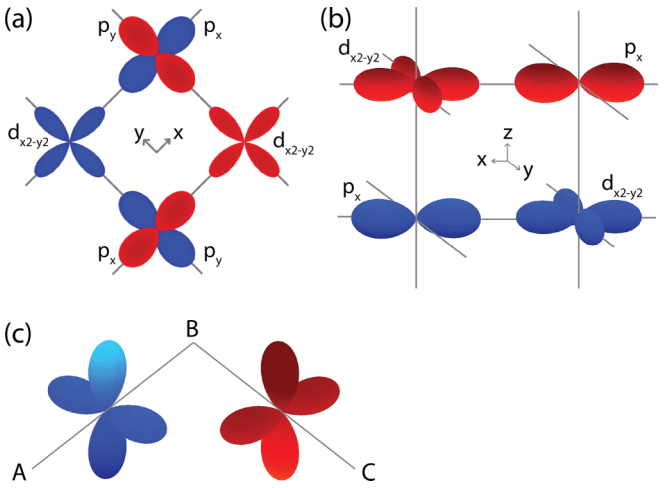

FIG. 6. Illustration of superexchange interactions between $CuCl_6$ octahedra in **1**. Superexchange interactions between neighboring copper ions (a) within a tetramer (see Fig. 1), (b) between adjacent tetramers, and (c) between adjacent ribbons of tetramers. In (c) the blue and red orbitals lie in a plane perpendicular to lines AB and BC, respectively, having no overlap. Different colors of $d_{x^2-y^2}$ orbitals correspond to different copper ions and match the color of the p orbitals they hybridize with.

1, which also occurs in other Jahn-Teller materials, such as CsO_2 [41] and $KCuF_3$ [42].

Figure 7 shows the tetramer of edge-sharing $CuCl_6$ octahedra. Due to the two crystallographically distinct copper ions, there are two different nearest-neighbor interactions within the tetramer: the interaction between Cu1 and Cu2 ions with the exchange constant J_1' and the interaction between two Cu2 ions (the exchange constant J_1). Figure 7(b) shows a top view of the edge-sharing plane of the tetramer, indicating the relevant

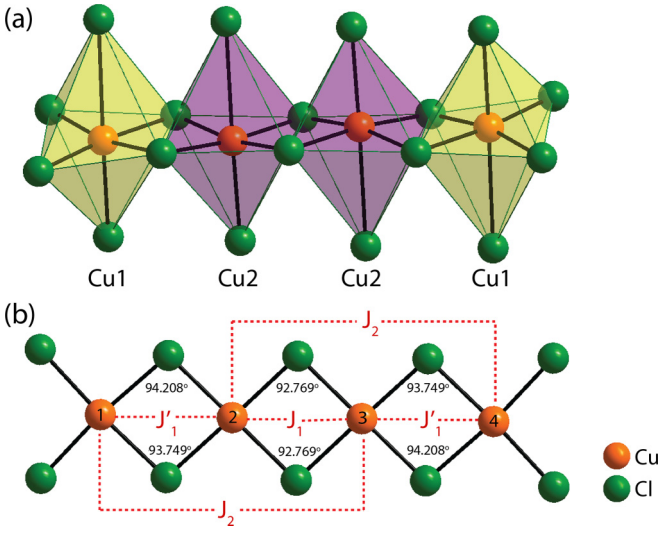

FIG. 7. (a) Tetramer of edge-sharing $CuCl_6$ octahedra. The yellow and purple shadings represent octahedra around the two crystallographically distinct copper atoms, Cu1 and Cu2, respectively. (b) Top view of the edge-sharing plane of the tetramer, indicating Cu-Cl-Cu angles, nearest-neighbor (J_1 and J_1'), and next-nearest-neighbor interactions (J_2).

Cu-Cl-Cu angles, θ, which are close to 90°. The weak FM exchange interactions cannot explain the origin of the observed magnetic susceptibility peak at 82 K. The only interaction in the tetramer that can lead to a nonmagnetic state with a large spin gap is the AFM interaction between next-nearest-neighbor spins with the exchange constant $J_2 > 0$. Strong next-nearest-neighbor interactions between Cu spins (∼100 K) were also found in Cu-O edge-sharing chains [43].

We propose a simple model in which the observed temperature dependence of the magnetic susceptibility of $CH_3NH_3Cu_2Cl_5$ can be understood. Herein, we neglect the relatively weak interactions between the tetramers (see Fig. 6). The spin Hamiltonian of an isolated tetramer is given by

$$H = J_1\mathbf{S}_2\cdot\mathbf{S}_3 + J_1'(\mathbf{S}_1\cdot\mathbf{S}_2 + \mathbf{S}_3\cdot\mathbf{S}_4) + J_2(\mathbf{S}_1\cdot\mathbf{S}_3 + \mathbf{S}_2\cdot\mathbf{S}_4), \quad (1)$$

where $\mathbf{S}_i$ ($i = 1,2,3,4$) is the spin on the ith site of the tetramer, J_1 and J_1' are the exchange constants between nearest-neighbor spins, and J_2 is the next-nearest-neighbor exchange constant (see Fig. 7). The 16 eigenstates of this Hamiltonian include the quintuplet of $S = 2$ states, where S is the total spin of the tetramer, with energy $E_2 = \frac{1}{4}(J_1 + 2J_1' + 2J_2)$, three triplets with $S = 1$ and two singlets with $S = 0$. The $S = 1$ states are either symmetric (s) or antisymmetric (a) with respect to $\mathbf{S}_2 \leftrightarrow \mathbf{S}_3$, $\mathbf{S}_1 \leftrightarrow \mathbf{S}_4$. The wave function for $S_z = +1$ becomes

$$|S = 1, S_z = +1\rangle_{s,a} = \alpha\downarrow\uparrow\uparrow\uparrow + \beta\uparrow\downarrow\uparrow\uparrow \pm\beta\uparrow\uparrow\downarrow\uparrow \pm\alpha\uparrow\uparrow\uparrow\downarrow, \quad (2)$$

where the ± sign corresponds to the symmetric/antisymmetric state. The energy of the symmetric state is given by $E_{1s} = \frac{1}{4}(J_1 - 2J_1' - 2J_2)$ and the energies of the two antisymmetric triplets are $E_{1a}^{\pm} = \frac{1}{4}[-J_1 \pm 2\sqrt{J_1^2 + (J_1' - J_2)^2}]$. On the other hand, the two singlet states have the symmetric wave functions

$$|S = 0, S_z = 0\rangle = \alpha(\downarrow\downarrow\uparrow\uparrow + \uparrow\uparrow\downarrow\downarrow) + \beta(\downarrow\uparrow\downarrow\uparrow + \uparrow\downarrow\uparrow\downarrow) + \gamma(\downarrow\uparrow\uparrow\downarrow + \uparrow\downarrow\downarrow\uparrow) \quad (3)$$

with $\alpha + \beta + \gamma = 0$. The energies of the $S = 0$ states are $E_0^{\pm} = \frac{1}{4}[-(J_1 + 2J_1' + 2J_2) \pm 2\sqrt{D}]$, where $D = (J_1 - J_1' - J_2)^2 + 3(J_1' - J_2)^2$. For the AFM next-nearest-neighbor interactions, $J_2 > 0$, and relatively weak FM nearest-neighbor interactions, $J_1, 2J_1' < 0$, the tetramer has the singlet ground state with energy E_0^-. When the relatively weak nearest-neighbor interactions are ignored, the ground state is the product of two singlet states formed on the pair of sites (1,3) and (2,4). The first excited state is a triplet with the energy E_{1s} or E_{1a}^-. The magnetic susceptibility per Cu^{2+} is given by

$$\chi = \frac{\mu_B^2}{k_B T}\langle S_z^2\rangle, \quad (4)$$

where μ_B is the Bohr magneton, k_B is the Boltzmann constant, T is the temperature, and $\langle S_z^2\rangle$ is the thermal average of the z component of the total spin of the tetramer given by

$$\langle S_z^2\rangle = \frac{2}{Z}(5e^{-\beta E_2} + e^{-\beta E_{1s}} + e^{-\beta E_{1a}^+} + e^{-\beta E_{1a}^-}), \quad (5)$$

where $Z = 5e^{-\beta E_2} + 3(e^{-\beta E_{1s}} + e^{-\beta E_{1a}^+} + e^{-\beta E_{1a}^-}) + e^{-\beta E_0^+} + e^{-\beta E_0^-}$ is the tetramer partition function. Figure 3 shows the comparison of the magnetic susceptibility of **1** (red circles

represent experimental data) with that of the isolated tetramer model calculated for $J_1 = J_1' = 0$ and $J_2 = +131.5$ K. We found that the shape of the susceptibility curve is almost solely determined by J_2: FM nearest-neighbor interactions with the strength of several tens of K have little effect on the theoretical susceptibility and therefore cannot be determined reliably from the susceptibility fit. The thin black line was obtained by normalizing the theoretical susceptibility so that it coincides with the experimental one at the maximum of the susceptibility. The good agreement shows that the simple model can reproduce the shape of the magnetic susceptibility. However, without a normalization factor, the theoretical susceptibility per mole of Cu^{2+} (thick blue line) is lower than the experimental one, especially at high temperatures. This can be understood as follows: the spin gap required to have the maximum of the susceptibility at 82 K is about 130 K. As a result, not all tetramer eigenstates are highly excited even at 300 K, which reduces the susceptibility. A large spin gap required to reproduce the low-temperature behavior of the susceptibility and the Curie-like behavior observed at high temperatures (see Fig. S9 [33]) suggest that the exchange constants in **1** might be temperature dependent, i.e., the crossover into the singlet state can be accompanied by a lattice deformation which increases the AFM interactions between spins through the spin-lattice coupling.

For future research, of particular interest would be the substitution of Cu with nonmagnetic ions. When other ions are substituted for magnetic ions in a spin gap system, the singlet ground state is disturbed so that staggered moments are induced around the impurities. If the induced moments interact through effective exchange interactions, which are mediated by intermediate singlet spins, exotic ground states appear or long-range order can arise [44]. Examples of impurity induced antiferromagnetic ordering in spin gap systems are $Cu_{1-x}Zn_xGeO_3$ [45], $Sr(Cu_{1-x}Zn_x)_2O_3$ [46], and $Pb(Ni_{1-x}Mg_x)_2V_2O_8$ [47]. We hypothesize that in our structure, replacing Cu by, for example, Fe might induce interactions between tetramers. As shown in Fig. 6, there are only very weak interactions between the Cl p_x orbital and the Cu $d_{x^2-y^2}$ orbitals. However, replacing Cu with Fe in the same structure will result in a significant interaction between the Cl p_x orbital and the Fe d_{xz} orbital. As a result, the neighboring tetramers will no longer be magnetically decoupled and a 2D magnetic lattice will be obtained.

IV. CONCLUSIONS AND OUTLOOK

In conclusion, we have synthesized and investigated the magnetic properties of a new methylammonium copper chloride compound: $CH_3NH_3Cu_2Cl_5$ (**1**). Our findings reveal that the hybrid grows with an alternative structural motif, not observed for organic-inorganic hybrids before. The crystal structure consists of inorganic sheets that are separated by organic cations. The inorganic $Cu_2Cl_5^-$ layers consist of a unique pattern of corner- and edge-sharing $CuCl_6$ octahedra. Our magnetic measurements reveal that the connectivity of JT-distorted octahedra gives rise to a broad maximum in the magnetic susceptibility at around 82 K. Moreover, our data show that **1** has a nonmagnetic ground state as supported by the ESR spectroscopic study. We propose a simple model in which the observed temperature dependence of the magnetic susceptibility of **1** can be understood based on strong AFM next-nearest-neighbor interactions in tetramers of edge-sharing $CuCl_6$ octahedra. The proposed model fits the shape of the broad maximum quite well, with exchange constants of about +130 K. Our findings show that the crystal chemistry of layered methylammonium copper chlorides allows a design beyond corner-sharing octahedra involving edge-sharing units, resulting in a 2D crystal structure with a singlet magnetic ground state.

ACKNOWLEDGMENT

M.E.K. was supported by The Netherlands Organisation for Scientific Research (NWO) Graduate Programme 2013, Grant No. 022.005.006.

[1] J. J. M. Steijger, E. Frikkee, L. J. De Jongh, and W. J. Huiskamp, Physica B **123**, 271 (1984).
[2] Y. Kimishima, J. Phys. Soc. Jpn. **49**, 62 (1980).
[3] L. J. De Jongh, A. C. Botterman, F. R. De Boer, and A. R. Miedema, J. Appl. Phys. **40**, 1363 (1969).
[4] M. F. Mostafa and R. D. Willett, Phys. Rev. B **4**, 2213 (1971).
[5] W. D. Van Amstel and L. J. De Jongh, Solid State Commun. **11**, 1423 (1972).
[6] R. D. Willett, F. H. Jardine, I. Rouse, R. J. Wong, C. P. Landee, and M. Numata, Phys. Rev. B **24**, 5372 (1981).
[7] C. Bellitto, P. Filaci, and S. Patrizio, Inorg. Chem. **26**, 191 (1987).
[8] F. Lipps, A. H. Arkenbout, A. Polyakov, M. Günther, T. Salikhov, E. Vavilova, H. Klauss, B. Büchner, T. M. Palstra, and V. Kataev, Low Temp. Phys. **43**, 1298 (2017).
[9] A. O. Polyakov, A. H. Arkenbout, J. Baas, G. R. Blake, A. Meetsma, A. Caretta, P. H. M. Van Loosdrecht, and T. T. M. Palstra, Chem. Mater. **24**, 133 (2012).
[10] W.-Q. Liao, Y. Zhang, C.-L. Hu, J.-G. Mao, H.-Y. Ye, P.-F. Li, S. D. Huang, and R.-G. Xiong, Nat. Commun. **6**, 7338 (2015).
[11] K. Yamada, T. Matsui, T. Tsuritani, T. Okuda, and S. Ichiba, Z. Naturforsch. **45a**, 307 (1990).
[12] D. B. Mitzi, C. A. Feild, W. T. A. Harrison, and A. M. Guloy, Nature (London) **369**, 467 (1994).
[13] D. B. Mitzi, S. Wang, C. A. Feild, C. A. Chess, A. M. Guloy, and N. Series, Science **267**, 1473 (1995).
[14] G. C. Papavassiliou, Prog. Solid State Chem. **25**, 125 (1997).
[15] Y. Takahashi, R. Obara, K. Nakagawa, M. Nakano, J.-Y. Tokita, and T. Inabe, Chem. Mater. **19**, 6312 (2007).
[16] G. C. Papavassiliou, Mol. Cryst. Liq. Cryst. **286**, 231 (1996).
[17] D. B. Mitzi, Chem. Mater. **8**, 791 (1996).
[18] A. Kojima, K. Teshima, Y. Shirai, and T. Miyasaka, J. Am. Chem. Soc. **131**, 6050 (2009).
[19] W. Zhang, M. Saliba, D. T. Moore, S. K. Pathak, M. T. Hörantner, T. Stergiopoulos, S. D. Stranks, G. E. Eperon, J. A. Alexander-Webber, A. Abate, A. Sadhanala, S. Yao, Y. Chen, R. H. Friend,

L. A. Estroff, U. Wiesner, and H. J. Snaith, Nat. Commun. **6**, 6142 (2015).
[20] Z.-K. Tan, R. S. Moghaddam, M. L. Lai, P. Docampo, R. Higler, F. Deschler, M. Price, A. Sadhanala, L. M. Pazos, D. Credgington, F. Hanusch, T. Bein, H. J. Snaith, and R. H. Friend, Nat. Nanotechnol. **9**, 687 (2014).
[21] F. Zhang, H. Zhong, C. Chen, X.-G. Wu, X. Hu, and H. Huang, ACS Nano **9**, 4533 (2015).
[22] G. Xing, N. Mathews, S. S. Lim, N. Yantara, X. Liu, D. Sabba, M. Grätzel, S. Mhaisalkar, and T. C. Sum, Nat. Mater. **13**, 476 (2014).
[23] H. Zhu, Y. Fu, F. Meng, X. Wu, Z. Gong, Q. Ding, M. V. Gustafsson, M. T. Trinh, S. Jin, and X.-Y. Zhu, Nat. Mater. **14**, 636 (2015).
[24] Y. Fang, Q. Dong, Y. Shao, Y. Yuan, and J. Huang, Nat. Photon. **9**, 679 (2015).
[25] J. B. Goodenough, Phys. Rev. **100**, 564 (1955).
[26] J. Kanamori, J. Phys. Chem. Solids **10**, 87 (1959).
[27] D. I. Khomskii and K. I. Kugel, Solid State Commun. **13**, 763 (1973).
[28] G. Heygster and W. Kleemann, Physica B **89**, 165 (1977).
[29] M. Matsumoto, H. Kuroe, T. Sekine, and T. Masuda, J. Phys. Soc. Jpn. **79**, 084703 (2010).
[30] M. Hase, K. Nakajima, S. Ohira-Kawamura, Y. Kawakita, T. Kikuchi, and M. Matsumoto, Phys. Rev. B **92**, 184412 (2015).
[31] I. Pabst, H. Fuess, and J. W. Bats, Acta Cryst. C **43**, 413 (1987).
[32] H. Arend, W. Huber, F. H. Mischgofsky, and G. K. Richter-Van Leeuwen, J. Cryst. Growth **43**, 213 (1978).
[33] See Supplemental Material at http://link.aps.org/supplemental/10.1103/PhysRevMaterials.2.064405 for optical images of crystals, asymmetric unit of **1**, magnetic measurements of **1** and **2**, additional ESR data (PDF), and the crystallographic information file of **1** (CIF).
[34] G. M. Sheldrick, *SHELX97, Program for Crystal Structure Refinement* (University of Göttingen, Göttingen, 1997).
[35] D. B. Mitzi, J. Chem. Soc., Dalton Trans. **0**, 1 (2001).
[36] W. G. Haije, J. A. L. Dobbelaar, and W. J. A. Maaskant, Acta Cryst. C **42**, 1485 (1986).
[37] H. Kageyama, K. Yoshimura, R. Stern, N. V. Mushnikov, K. Onizuka, M. Kato, K. Kosuge, C. P. Slichter, T. Goto, and Y. Ueda, Phys. Rev. Lett. **82**, 3168 (1999).
[38] S. Miyahara, F. Becca, and F. Mila, Phys. Rev. B **68**, 024401 (2003).
[39] M. Jaime, R. Daou, S. A. Crooker, F. Weickert, A. Uchida, A. E. Feiguin, C. D. Batista, H. A. Dabkowska, and B. D. Gaulin, Proc. Natl. Acad. Sci. USA **109**, 12404 (2012).
[40] B. S. Shastry and B. Sutherland, Physica B **108**, 1069 (1981).
[41] S. Riyadi, B. Zhang, R. A. de Groot, A. Caretta, P. H. M. van Loosdrecht, T. T. M. Palstra, and G. R. Blake, Phys. Rev. Lett. **108**, 217206 (2012).
[42] S. Kadota, I. Yamada, S. Yoneyama, and K. Hirakawa, J. Phys. Soc. Jpn. **23**, 751 (1967).
[43] Y. Mizuno, T. Tohyama, S. Maekawa, T. Osafune, N. Motoyama, H. Eisaki, and S. Uchida, Phys. Rev. B **57**, 5326 (1998).
[44] M. Fujisawa, A. Asakura, S. Okubo, H. Ohta, S. Nishihara, T. Akutagawa, T. Nakamura, and Y. Hosokoshi, J. Phys.: Conf. Ser. **150**, 042034 (2009).
[45] M. Hase, I. Terasaki, Y. Sasago, K. Uchinokura, and H. Obara, Phys. Rev. Lett. **71**, 4059 (1993).
[46] M. Azuma, Y. Fujishiro, M. Takano, M. Nohara, and H. Takagi, Phys. Rev. B **55**, R8658 (1997).
[47] Y. Uchiyama, Y. Sasago, I. Tsukada, K. Uchinokura, A. Zheludev, T. Hayashi, N. Miura, and P. Böni, Phys. Rev. Lett. **83**, 632 (1999).